ADVANCED FUNCTIONAL MATERIALS
www.afm-journal.de

Reconstruction of Conformal Nanoscale MnO on Graphene as a High-Capacity and Long-Life Anode Material for Lithium Ion Batteries

Yongming Sun, Xianluo Hu, Wei Luo, Fangfang Xia, and Yunhui Huang**

To tackle the issue of inferior cycle stability and rate capability for MnO anode materials in lithium ion batteries, a facile strategy is explored to prepare a hybrid material consisting of MnO nanocrystals grown on conductive graphene nanosheets. The prepared MnO/graphene hybrid anode exhibits a reversible capacity as high as 2014.1 mAh g^{-1} after 150 discharge/charge cycles at 200 mA g^{-1}, excellent rate capability (625.8 mAh g^{-1} at 3000 mA g^{-1}), and superior cyclability (843.3 mAh g^{-1} even after 400 discharge/charge cycles at 2000 mA g^{-1} with only 0.01% capacity loss per cycle). The results suggest that the reconstruction of the MnO/graphene electrodes is intrinsic due to conversion reactions. A long-term stable nanoarchitecture of graphene-supported ultrafine manganese oxide nanoparticles is formed upon cycling, which yields a long-life anode material for lithium ion batteries. The lithiation and delithiation behavior suggests that the further oxidation of Mn(II) to Mn(IV) and the interfacial lithium storage upon cycling contribute to the enhanced specific capacity. The excellent rate capability benefits from the presence of conductive graphene and a short transportation length for both lithium ions and electrons. Moreover, the as-formed hybrid nanostructure of MnO on graphene may help achieve faster kinetics of conversion reactions.

1. Introduction

Rechargeable lithium ion batteries (LIBs) have been intensively pursued during the past decade. Currently, a major research direction is the design, fabrication, and exploitation of various LIB electrode materials with high reversible capacity, good rate capability, long cycle life, and low cost.[1–5] Recently, transition metal oxides, including CoO,[6–9] Co_3O_4,[10,11] Fe_2O_3,[12–14] Fe_3O_4,[15–17] SnO_2,[18,19] NiO,[20,21] Mn_3O_4,[22,23] and MoO_2,[24–27] have been intensively exploited as promising anode materials because of their high theoretical specific capacities. Among the various transition metal oxides investigated for LIBs, MnO is an attractive anode material due to a low conversion potential, low voltage hysteresis (<0.8 V), high density (5.43 g cm^{-3}), low cost, environmental benignity, and the high abundance of Mn.[28–41] However, there are still challenges in the application of MnO to practical LIBs, especially the obstacles of poor cycling stability and inferior rate capability. The drastic volume changes during the repeated lithium insertion/extration processes give rise to pulverization, which results in the breakdown of electrical connection of such anode materials from current collectors and rapid capacity fading upon cycling. In addition, MnO-based electrodes have poor rate capability as a result of poor electronic conductivity. Therefore, it still remains a great challenge to maintain the mechanical strength and good conductivity of MnO electrodes over continuous discharge/charge cycles, in order to achieve high performances. To the best of our knowledge, MnO-based anode materials with long cycle life (e.g., >300 cycles), high reversible capacity (e.g., >1000 mAh g^{-1}), and excellent rate capability (e.g., >800 mAh g^{-1} at 2000 mA g^{-1}) have never been reported for lithium storage to date. Also, there has been no report on the detailed structural analysis of MnO-based electrodes over continuous discharge/charge cycles.

Graphene, a two-dimensional material with exceptionally high crystallity and electronic qualities, has recently attracted enormous research interest in materials science.[42] Owing to its superior conductivity, large surface area, structural flexibility, and chemical stability, various transition metal oxide/graphene hybrids have been widely explored for energy-storage applications, and indeed such hybrids do exhibit enhanced electrochemical performance.[12,17,19,22,25,28,43–45] Thus, the strategy of preparing transition metal oxides/graphene composites may be an effective route to obtain enhanced lithium-storage properties. The primary advantages of those composites as anode materials in LIBs are their high reversible capacity and good rate capability. Moreover, the capacity retention is also improved in comparison to that of their pristine counterparts.[12,17,19,22,25,28,43,44] However, maintenance of electrode integrity over continuous discharge/charge cycles is far away from realization. The cycle life of transition metal oxide/graphene hybrid electrodes is often limited. The reported capacity retention is mostly obtained below 100 charge/discharge cycles, and is nowhere

Y. M. Sun, Prof. X. L. Hu, W. Luo, F. F. Xia
Prof. Y. H. Huang
State Key Laboratory of Material Processing and Die & Mould Technology
College of Materials Science and Engineering
Huazhong University of Science and Technology
Wuhan 430074, P. R. China
E-mail: huxl@mail.hust.edu.cn; huangyh@mail.hust.edu.cn

DOI: 10.1002/adfm.201202623

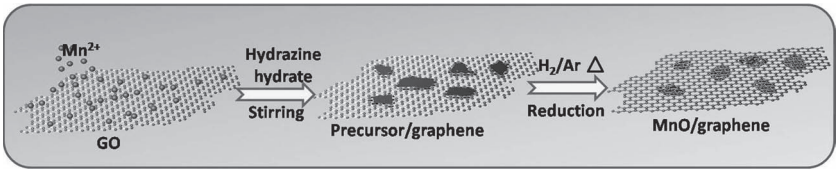

Figure 1. Schematic illustration of the formation of the MnO/graphene composite.

near enough for practical implementation. Thus, to meet ever-increasing demand, it is highly desirable to develop high-performance anode materials for LIB applications.

Herein, we report a facile solution-based method combined with a subsequent reduction process for the large-scale fabrication of a MnO/graphene nanocomposite. As expected, the hybrid MnO/graphene electrode exhibits high lithium-storage capacity, impressive rate capability, and superior cyclability, due to the synergetic effects of graphene and MnO nanocrystals. Importantly, the reconstruction of conformal MnO on the graphene nanosheets during the repeated lithium insertion/extraction processes contributes to a superior electrochemical performance.

2. Results and Discussion

The general process for the fabrication of MnO/graphene composite is illustrated in **Figure 1**. Typically, manganese acetate and graphene oxide (GO) reacted with hydrazine hydrate in solution to produce a Mn-based precursor/graphene composite (Figure S1–4, Supporting Information). The MnO/graphene hybrid was finally obtained by annealing the intermediate product at 500 °C for 5 h in a reducing H_2/Ar atmosphere. **Figure 2** shows the X-ray diffraction (XRD) pattern of the product. All the diffraction peaks could be readily indexed to a pure cubic phase [space group: $Fm\bar{3}m$ (225)] of MnO (JCPDS no. 07–0230). Under the same thermal treatment conditions, pure MnO was also obtained in the absence of graphene (Figure S5, Supporting Information).

X-ray photoelectron spectroscopy (XPS) was employed to analyze the information on the surface electronic state and the composition of the products. As shown in **Figure 3**a, the peaks arising from Mn (2s, $2p_{1/2}$, $2p_{3/2}$, 3s, and 3p) and O (1s) in the survey XPS spectrum can be assigned to MnO. Meanwhile, the peak labeled C 1s originates from the graphene nanosheets. The Mn 2p peak was further examined by high-resolution XPS analysis (Figure 3b). The two signals at 641.2 and 652.8 eV may be attributed to Mn (II) $2p_{3/2}$ and $2p_{1/2}$, respectively, characteristic of MnO.[46] The high-resolution C 1s spectrum is shown in Figure 3c. The strong C 1s peak at 284.4 eV corresponds to graphitic carbon in graphene, while the weaker ones arising from the oxygenated carbon atoms (C–O at 286.2 eV; C=O, 287.9 eV; O–C=O, 289.0 eV)[47] indicate the deoxygenation process accompanying the reduction of GO. A small O 1s peak at 532.0 eV is observed, which indicates the existence of residual O^{2-} species bonded with C atoms in graphene (Figure 3d).[48]

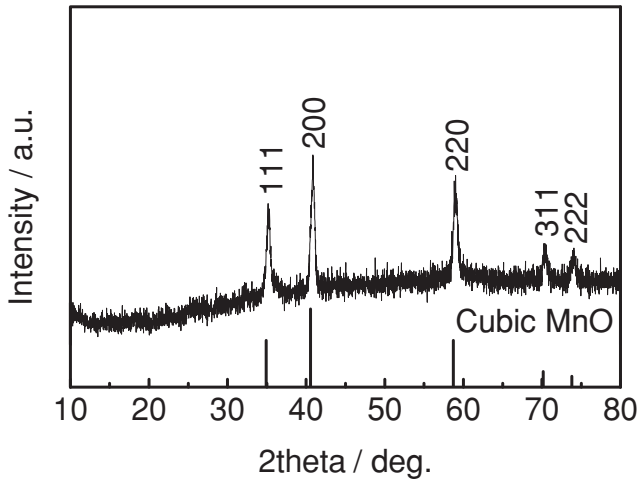

Figure 2. Typical XRD pattern of the resultant MnO/graphene hybrid.

The morphology and microstructure of the MnO/graphene product were investigated by field-emission scanning microscope (FESEM) and transmission electron microscopy (TEM). **Figure 4**a,b show typical FESEM images of the MnO/graphene product. Evidently, a large number of porous MnO nanosheets with a diameter of ca. 50–300 nm and a thickness of ca. 10 nm are well dispersed on the graphene sheets. The uniform and intimate contact between MnO and graphene nanosheets may prevent both the aggregation of MnO particles and the restacking of graphene nanosheets. The corresponding energy-dispersive X-ray (EDX) spectrum (Figure S6, Supporting Information) suggests the existence of Mn, O, and C in the resultant MnO/graphene hybrid, which is also consistent with the XRD and XPS results (Figure 2 and 3). In contrast, there is no significant difference in the morphology of the bare MnO and its precursor (Figure S4 and S7, Supporting Information). Figure 4c shows a typical bright-field TEM image at a low magnification for the MnO/graphene product. The MnO nanosheets are well attached to the graphene sheets, even after ultrasonication for 0.5 h to disperse the sample for TEM characterization. The corresponding selected-area electron diffraction (SAED) pattern reveals that the obtained MnO nanosheets are polycrystalline (inset of Figure 4c). Figure 4d shows a high-resolution TEM (HRTEM) image of the MnO/graphene product. The well-resolved periodic lattice fringe with an interplanar distance of ca. 2.6 Å comes from the (111) plane of cubic MnO. Additionally, a nanolayer of several nanometers on the surface of the MnO nanocrystals can be clearly observed, with the interplanar spacing of ca. 0.37 nm, which corresponds to the separation between (002) lattice planes of graphite. Thus, a unique nanoarchitecture of graphene-supported MnO can be readily identified.

Raman spectra were recorded to investigate the structural changes from GO to graphene (Figure S8, Supporting Information). The characteristic D band and G band are observed for both the MnO/graphene and GO products. A reduced size of the sp^2 domains and the creation of new graphitic domains with smaller sizes can be identified during the reduction reaction by the increasing value of the D/G intensity ratio in the MnO/graphene hybrid in comparison to that of GO.[49] Additionally, peaks at 352 and 639 cm^{-1} are assigned to manganese

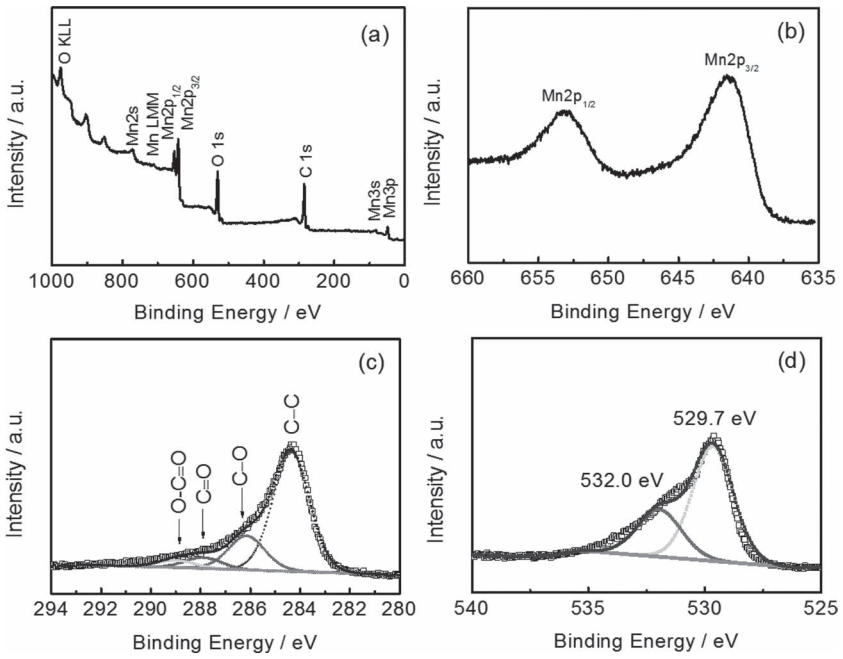

Figure 3. XPS spectra for the as-prepared MnO/graphene composite: a) survey spectrum and high-resolution b) Mn 2p, c) C 1s, and d) O 1s spectra.

oxide. The content of graphene in the MnO/graphene product is evaluated to be about 17.4 wt% by thermogravimetric analysis (TGA; Figure S9, Supporting Information). The MnO/graphene product is further characterized by nitrogen adsorption and desorption isotherms at 77 K (Figure S10, Supporting Information). The MnO/graphene hybrid has a specific surface area (Brunauer–Emmett–Teller; BET) of 50.3 m^2 g^{-1} with a pore volume of 0.33 cm^3 g^{-1} and an average Barrett–Joyner–Halenda (BJH) pore diameter of 2.6 nm. The high specific surface area and the nanoporous nature of the MnO/graphene composite are very advantageous for lithium ion and electron transport.

The electrochemical lithium-storage properties of the as-formed MnO/graphene nanocomposite have been further explored. As shown in **Figure 5**a, b, the initial reversible capacity is around 890.7 mAh g^{-1} at a current density of 200 mA g^{-1}. After 150 discharge/charge cycles, however, the MnO/graphene electrode shows a high reversible capacity of 2014.1 mAh g^{-1}. This gravimetric capacity is over five times higher than the theoretical capacity of graphite (≈372 mAh g^{-1}). To the best of our knowledge, this is the highest reversible capacity of the previously reported transition metal oxides and their derivative composites; it is also much higher than the theoretical capacities of both MnO (≈756 mAh g^{-1}) and graphene (≈744 mAh g^{-1}). Such a high specific capacity indicates high accessibility for lithium insertion and extraction in the as-prepared electrodes. Importantly, the MnO/graphene nanocomposite presents outstanding rate capability (Figure 5c). Even at a current density of 3000 mA g^{-1}, the specific capacity is as high as 625.8 mAh g^{-1}, still much higher than the theoretical capacity of graphite. A capacity of 921.7 mAh g^{-1} at 200 mA g^{-1} was retained after 80 discharge/charge cycles at various current densities, which indicates good structural stability of the MnO/graphene composite. Furthermore, the MnO/graphene hybrid electrodes exhibit satisfactory cycling performance even at high current density. The specific capacity of the composite is 843.3 mAh g^{-1} after 400 discharge/charge cycles at 2000 mA g^{-1}, with a coulombic efficiency of ca. 99% and only 0.01% capacity loss per cycle (Figure 5d,e). It is believed that the lithium ions can rapidly insert and extract from the active materials and retain a stable structure even after continuous discharge/charge cycles. For comparison, we also explored the electrochemical performance of the bare MnO particles. The MnO electrode exhibits very low capacity and poor cyclability (Figure S11, Supporting Information).

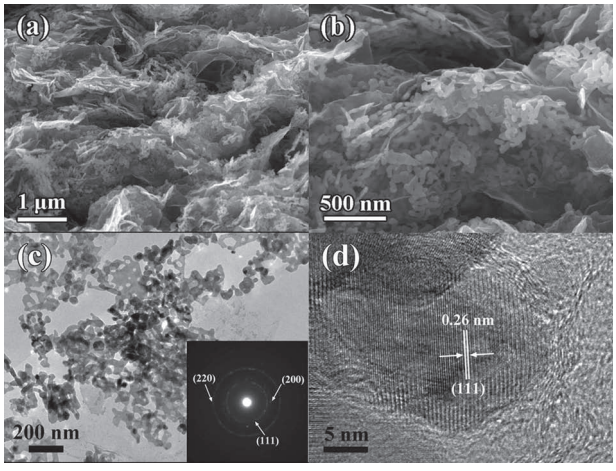

Figure 4. a,b) FESEM, c) TEM, and d) HRTEM images of the as-synthesized MnO/graphene hybrid. The inset in (c) is the corresponding SAED pattern.

To understand the superior electrochemical performance of the hybrid MnO/graphene electrode, further studies were carried out to investigate the physical/chemical behavior during the discharge/charge cycling. **Figure 6**a shows representative cyclic voltammetry (CV) curves of the MnO/graphene electrode for the initial six cycles at a scan rate of 0.2 mV s^{-1} in the voltage range of 0.01–3V vs. Li. In the first cycle, an irreversible reduction peak at around 0.68 V corresponds to the irreversible reduction of electrolyte and the formation of a solid electrolyte interphase (SEI) layer.[28,29,32,38] Additionally, the sharp cathodic peak at ca. 0.18 V corresponds to the complete reduction of Mn^{2+} to Mn^0, which shifts significantly to 0.42 V in the subsequent cycles. The lithiation voltage in the second and following cycles (≈0.42 V) is higher than that in the first cycle (≈0.18 V), probably due to the improved kinetics of the MnO/graphene electrode resulting from a microstructure alteration after the first lithiation.[29,32,37,38,50] The origin the improved kinetics has been discussed in terms of the surface energy and the amorphization effect in the case of RuO_2.[50] The main oxidation peak at about 1.32 V could be ascribed to the oxidation of Mn^0

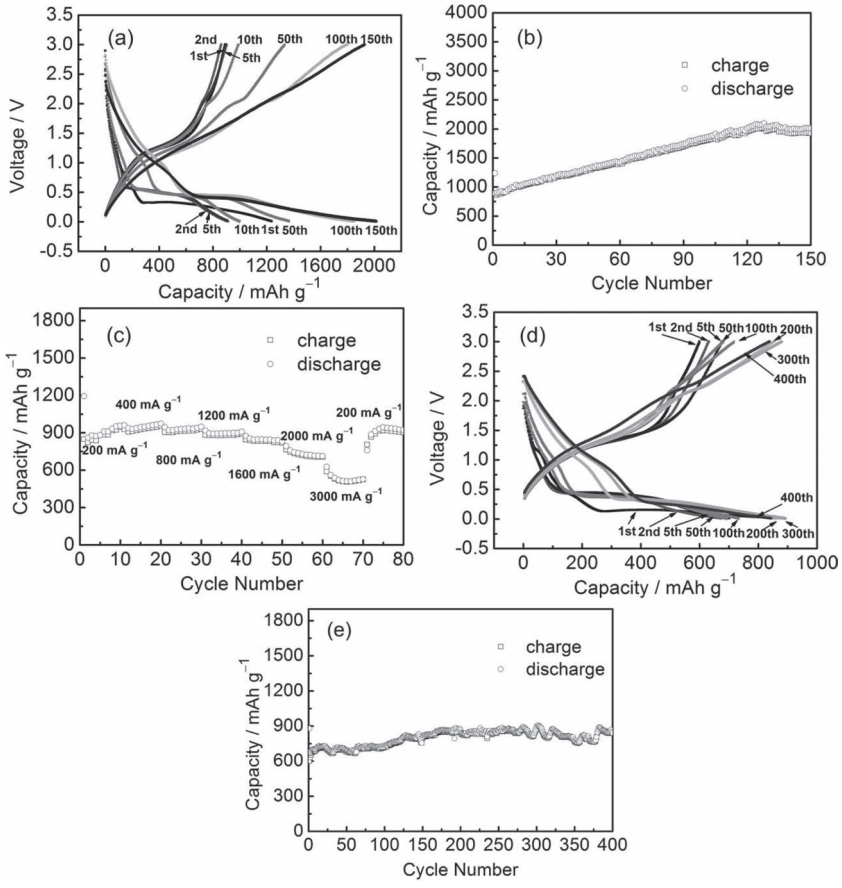

Figure 5. a) Discharge and charge voltage profiles of the obtained MnO/graphene product at a current density of 200 mA g^{-1}. b) Cycling performance of the prepared MnO/graphene hybrid electrode cycled at 200 mA g^{-1} and c) at various current densities of 200, 400, 800, 1200, 1600, 2000, and 3000 mA g^{-1}. d) Discharge and charge curves at a current density of 2000 mA g^{-1}. e) Cycling performance of the MnO/graphene electrodes at 2000 mA g^{-1}. All carried out in the voltage range 3–0.01 V vs. Li.

to Mn^{2+} in the cathodic process.[36] It is worth pointing out that an oxidation peak at ca. 2.10 V becomes evident gradually upon cycling, which indicates that the Mn^{2+} ions in MnO/graphene hybrid could be re-oxidized to a higher oxidation state.[51] This phenomenon is also reflected in the capacity vs. voltage curves extracted from the galvanostatic profiles. As shown in Figure 5a, a charge slope at around 2.10 V appears, gradually broadens, and finally transforms into a long plateau upon cycling, indicating an ever-increasing capacity and Li^+ reactivity. In the 50th discharge/charge curve, there is a discharge plateau at around 0.42 V and two charge plateaus at 1.32 and about 2.10 V, consistent with those of manganese oxides with higher oxidation states (Mn^{4+}).[52] XPS measurements were used to examine the valence states of the Mn ions in the hybrid electrode after 150 discharge/charge cycles at 200 mA g^{-1}. As shown in **Figure 7**, the XPS spectrum of the cycled material shows that the Mn 2p peaks are broader and weaker than that of the fresh MnO/graphene hybrid (shown in Figure 3b). Two characteristic peaks for Mn $2p_{1/2}$ and $2p_{3/2}$ are observed at about 654.4 and 642.5 eV, corresponding to Mn^{4+}.[46] In contrast, the Mn^{2+} ions in bare MnO could not be re-oxidized to a higher oxidation state, as evidenced in Figure 6b. It is worth noting that the manganese oxides, such as MnO_2, Mn_3O_4, and MnO, often undergo the reversible conversion reaction between MnO and metallic Mn.[31] Therefore, the high-oxidation end product after recharge to 3.0 V indicates the enhanced kinetics of conversion reactions for the as-prepared electrodes. Moreover, the second and onward CV curves remain steady, which indicates the highly reversible conversion reaction of MnO/graphene hybrid, instead of the poor reversibility of bare MnO (Figure 6b). The electrochemical impedance spectra of the electrodes for the as-prepared MnO/graphene and the bare MnO over the frequency range from 100 kHz to 0.1 Hz were investigated (**Figure 8**). Each of the Nyquist plots consists of a depressed semicircle (at high frequency) attributed to the charge-transfer reaction at the electrolyte/electrode interface and a linear Warburg part (at a low frequency) attributed to the diffusion of the lithium ions in the bulk of the electrode. The MnO/graphene electrode exhibits a much lower resistance than the bare MnO electrode. The reduction of resistance might be attributed to the existence of graphene. The electrochemical impedance spectra of the MnO/graphene electrode after different discharge/charge cycles at 200 mA g^{-1} were also measured (**Figure 9**). The Nyquist plots of the sample for the 1st and 10th cycles are similar. The charge-transfer resistance for the 10th cycle was obviously smaller than that in the 1st cycle, which indicates the activation and improved kinetics of the reaction upon cycling. It has been widely observed that Mn^{2+} ions in well-designed manganese oxide electrodes could be further oxidized to a higher oxidation state (>2) due to the fast Li reaction kinetics.[22,51,53] For instance, Guo et al. reported that Mn^{2+} ions could be re-oxidized to a higher oxidation state in amorphous MnO_x/carbon electrodes due to the synergistic effects of carbon and the amorphous structure.[51] For the Mn_3O_4/graphene and MnO_2/carbon nanotube nanocomposites, a charge plateau at around 2.10 V could be observed in the capacity–voltage curves, indicating a higher oxidation state (>2) of manganese in the end product.[22,52] For the MnO/graphene electrodes, the improved Li-reaction kinetics is confirmed by the lower charge-transfer resistance than that of the bare MnO electrodes (Figure 8). Meanwhile, the amorphization and the formation of ultrafine nanoparticles upon cycling improve the conversion reaction kinetics, as evidenced by the lower charge-transfer resistance upon cycling (Figure 9). Thus, it is reasonable that Mn^{2+} ions in the MnO/graphene electrode could be re-oxidized to a higher oxidation state due to the improved reaction kinetics.

The morphology of the MnO/graphene electrode over continuous discharge/charge cycles was studied. After one discharge/charge cycle at 2000 mA g^{-1}, the overall shape of the anode material is preserved, while a complete collapse of the initial

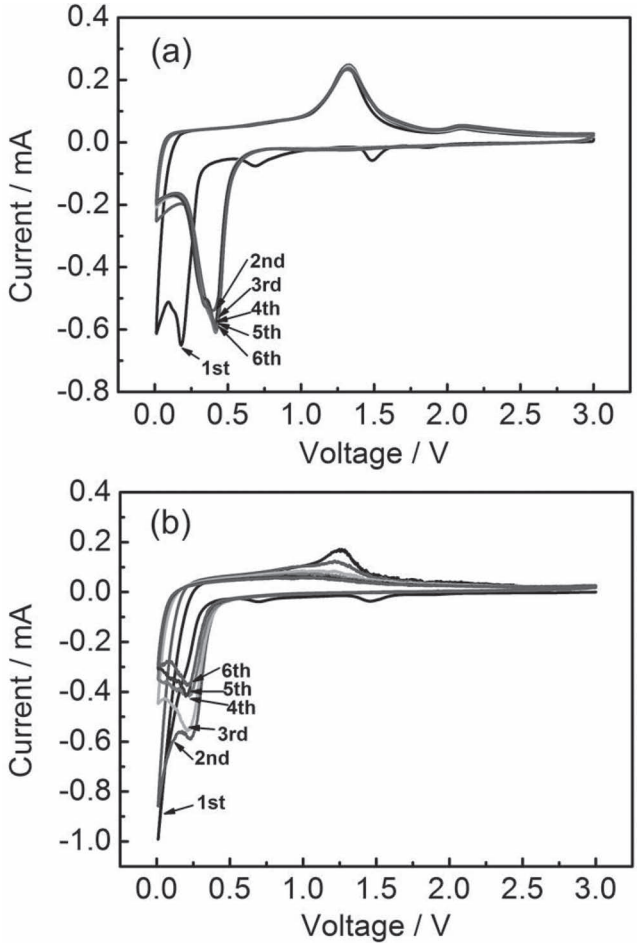

Figure 6. Representative CV curves of a) the synthesized MnO/graphene hybrid and b) the bare MnO obtained at a scan rate of 0.2 mV s^{-1} in the voltage range of 3–0.01 V vs. Li.

MnO nanosheets into ultrafine MnO nanoparticles is observed (**Figure 10**a–d and **11**a,b). More interestingly, the morphology of the anode material changes completely, and the graphene-supported nanosheets transform into graphene-supported ultrafine nanoparticles after 400 discharge/charge cycles. An interconnected structure is self-formed based on the three-dimensional graphene frame (Figure 10e,f and 11c,d). The aggregation of active nanoparticles does not occur in the present hybrid electrode. Ultrafine manganese oxide nanoparticles (≈2 nm) are homogeneously dispersed on the graphene matrix, as evidenced by the SEM, TEM, EDX, and elemental mapping results (Figure 10e,f, 11c,d, **12**, and Figure S12 in the Supporting Information). The MnO/graphene electrode before electrochemical cycling has a unique multilayer sandwich structure (Figure S13a, Supporting Information). The graphene nanosheets function as the sandwiched current collector and stabilizer, with an active MnO interlayer between the graphene layers. Thus, the electrical conductivity, structural flexibility, and chemical stability

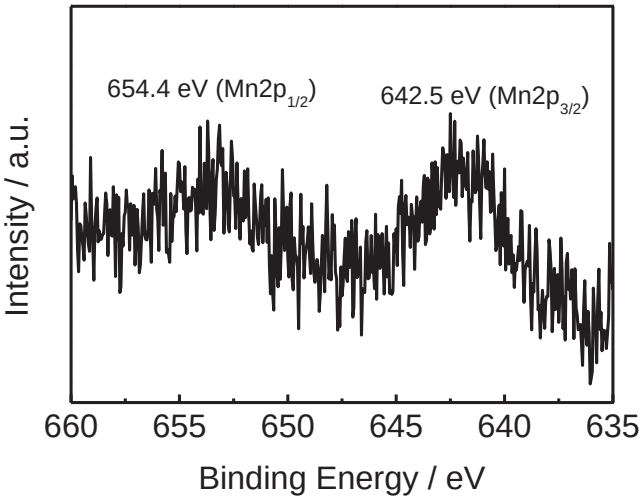

Figure 7. High-resolution Mn 2p XPS spectrum of the MnO/graphene hybrid electrode after 150 discharge/charge cycles at 200 mA g^{-1}.

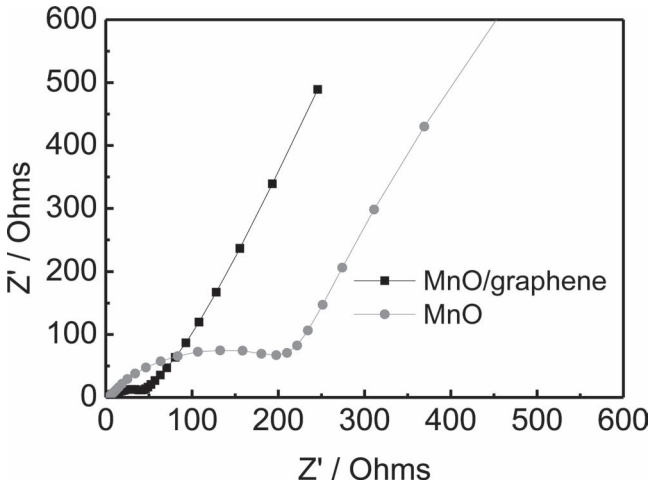

Figure 8. Electrochemical impedance spectra of the electrodes for the MnO/graphene hybrid and bare MnO.

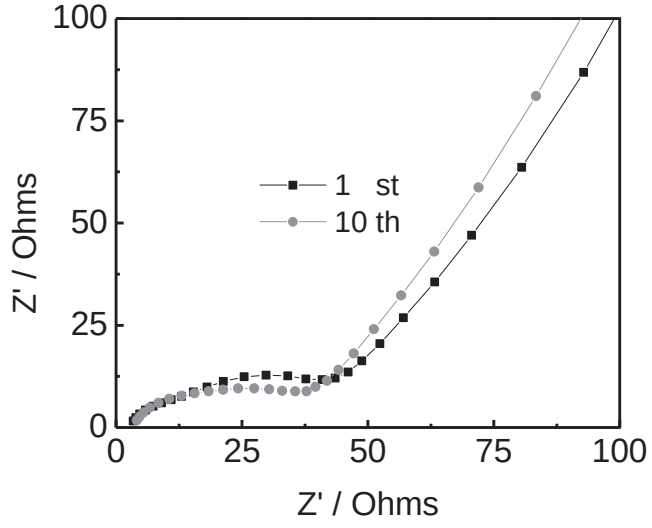

Figure 9. Electrochemical impedance spectra of the MnO/graphene electrode after different discharge/charge cycles at 200 mA g^{-1} over the frequency range from 100 kHz to 0.1 Hz.

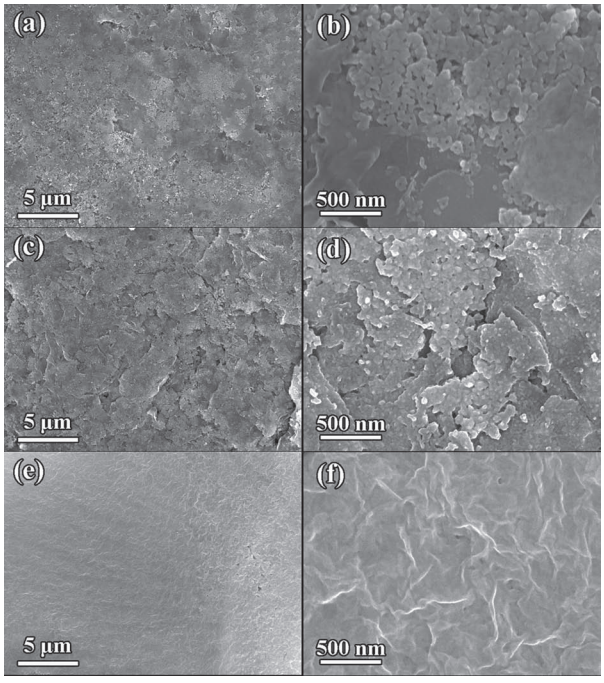

Figure 10. FESEM images of the MnO/graphene electrodes observed from the surface: a,b) the initial electrode, c,d) the electrode after one discharge/charge cycle, and e,f) the electrode after 400 discharge/charge cycles at 2000 mA g^{-1}.

of the hybrid electrode are greatly enhanced. This enhanced conductivity results in the significant enhancement of the utilization efficiency of the active manganese oxide and the discharge/charge ability at large current densities. The graphene layers can not only prevent the volume expansion/contraction but also limit the aggregation of the active materials effectively during Li^+ insertion and extraction upon cycling. After 400 discharge/charge cycles at 2000 mA g^{-1}, "electrochemical sintering" happens, which results in loss of porosity between the graphene layers, and hence a more dense structure is generated (Figure S13, Supporting Information). Indeed, a similar behavior has been observed in porous Ge electrodes.[54] In the reconstructed electrode, the initial MnO nanosheets may melt into a thinner film composed of ultrafine manganese oxide nanoparticles that are uniformly loaded on or sandwiched between the graphene layers. Thus, the proportion of the total active materials on the surface of graphene increases. Despite the loss of the initial morphology, the active manganese oxide nanoparticles formed by reconstruction may connect electrochemically with the graphene matrix more closely and facilitate charge transfer. A schematic illustration of the structural and morphological evolution for the MnO/graphene electrode is shown in Figure S14 (Supporting Information). Because of the high conductivity of graphene and the intimate contact between the active manganese oxide and graphene, the charge carriers can conduct back and forth effectively and rapidly from the active materials to the current collector through the conducting graphene matrix, which therefore leads to high specific capacity and rate capability.

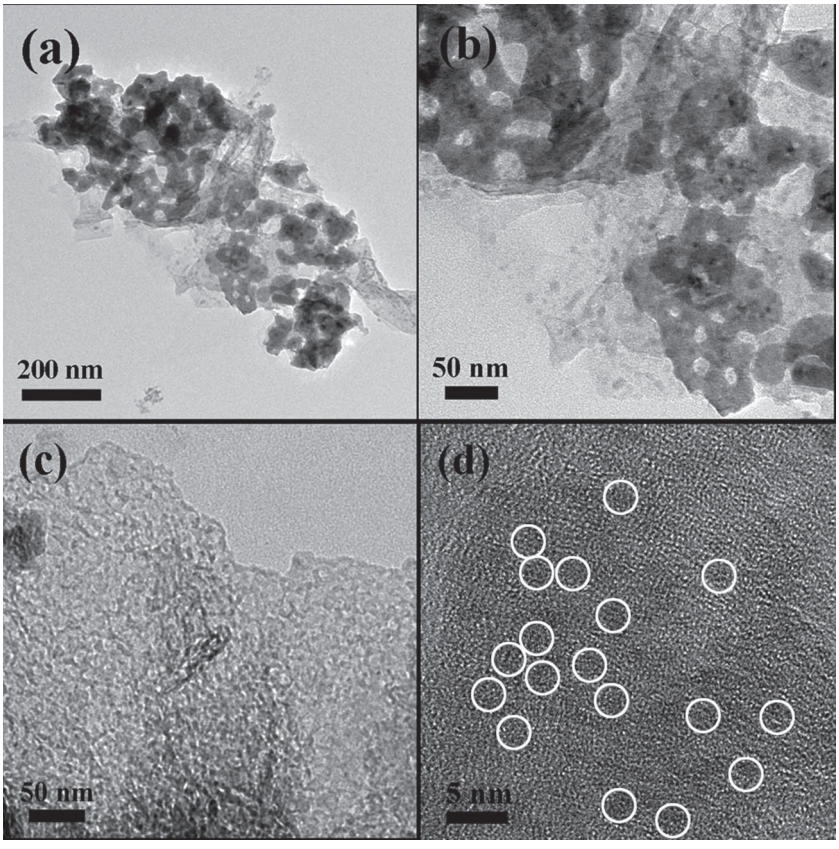

Figure 11. TEM images of the MnO/graphene electrodes after a,b) 1 and c,d) 400 discharge/charge cycles at 2000 mA g^{-1}.

The structural integrity of the electrodes is considered to be one of the most important factors in ensuring good cyclability over continuous discharge/charge cycles. Based on the conversion-reaction mechanism of transition metal oxides, the severe volume change that occurs upon Li^+ insertion and extraction causes mechanical degradation. The collapse and reconstruction of the initial structures of the active materials are inevitable after continuous discharge/charge cycles, usually resulting in a short cycle life especially at high charge/discharge rates. For the present hybrid MnO/graphene electrodes, the graphene nanosheets, loaded with the active manganese oxide nanoparticles, connect with each other to form a three-dimensional framework with good flexibility and mechanical stability, and thus can accommodate volume expansion/contraction during the Li^+ insertion/extraction processes. Meanwhile, the manganese oxide nanoparticles conformally anchored on the graphene nanosheets can avoid the restacking of the graphene, to retain a large specific surface area and an open three-dimensional conducting framework during the insertion and extraction of Li^+ upon cycling. Importantly, the transition of electrode materials during cycling is electrochemically driven and the

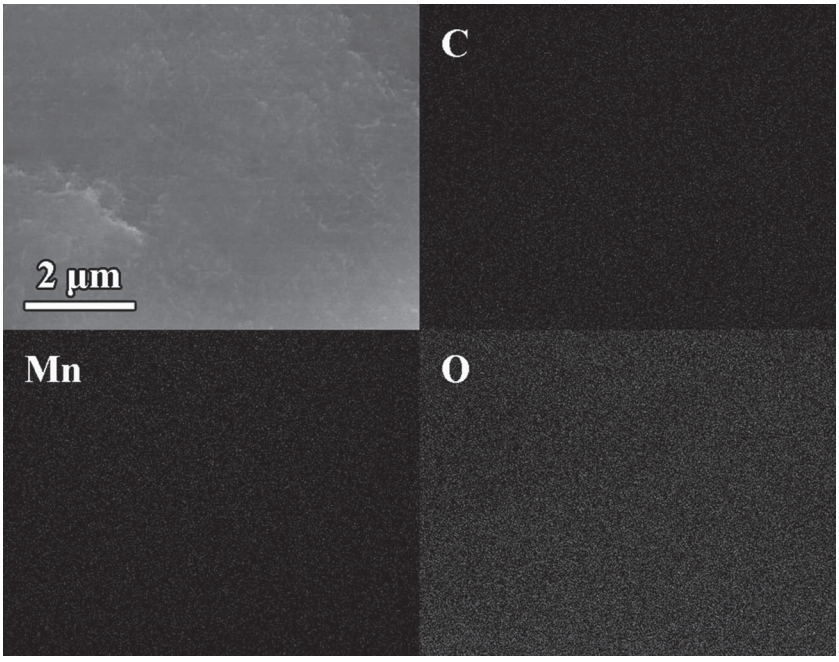

Figure 12. FESEM image and corresponding elemental mapping of C, Mn, and O in the MnO/graphene hybrid electrode after 400 discharge/charge cycles at 2000 mA g^{-1}.

reconstructed electrode can keep a stable structure over a large number of discharge/charge cycles. Such a stable interconnected three-dimensional electrode nanostructure based on the frame of graphene is very preferable; it not only improves the electronic conductivity but also maintains the structural integrity of the electrode even over a great many discharge/charge cycles (Figure 10e,f).

It is noted that the capacity increases gradually over the initial cycling, especially at low current densities. The increased capacity could be due to the interfacial Li storage (as proposed by Maier and co-workers.[55,56] and Tarascon and co-workers[57]) and high-oxidation state products, evidenced by the XPS results (Figure 7). As shown in Figure 5b, when discharged and charged at 200 mA g^{-1}, the capacity increases gradually until the 120th cycle and remains stable in the following cycles. The electrochemically driven reconstruction of the hybrid MnO/graphene electrodes may help enhance the electrochemical activity, thus leading to an improved specific capacity. Accompanied by the formation of the reconstructed nanostructure, more Mn^{2+} ions could be re-oxidized to a higher oxidation state upon cycling, leading to an ever-increasing capacity. Meanwhile, there is an increase in the proportion of the total active materials on the surface of graphene, which makes the electrochemical reactivity of the active particles more and more important.[6] Also, the reduced size of the particles leads to an increase in specific surface area, which may enhance the ability of interfacial lithium storage. However, this steady increase in capacity is not unceasing. The structure of the reconstructed electrode strikes a balance after a certain number of discharge/charge cycles (120 cycles at 200 mA g^{-1}) and the specific capacity starts to remain stable. There is also a possibility that the increased capacity over cycling might arise from the improved Li-diffusion kinetics by an activation process associated with partial crystallinity degradation of the electrode to a disordered or amorphous-like structure during cycling. A similar phenomenon is also reported in other graphene-based composites.[25,43]

The high specific capacity, superior cyclability, and good rate capability of the resultant MnO/graphene composite is unprecedented among graphene-based hybrid materials, which may be attributed to the synergistic effects of the nanohybridzation: an interconnected three-dimensional graphene framework loaded with manganese oxide nanoparticles. This graphene matrix is beneficial to reduce the inner resistance of the LIBs and stabilize the electronic and ionic conductivity, thus leading to a high specific capacity and good rate capability. Meanwhile, the stable structure of the reconstructed electrode contributes to a long cycle life.

3. Conclusions

In summary, we have demonstrated that the hybrid MnO/graphene electrodes exhibit superior electrochemical performances, featuring high reversible capacity, excellent rate capability and long cycle life. Our strategy to employ the synergistic couple of MnO and graphene is successful in designing advanced anode materials, enabling the applications of conversion-electrode materials with high energy density, power density, and long lifespan in LIBs. For the first time, Li^+ insertion/extraction-driven reconstruction of conversion electrodes on graphene has been demonstrated. Inspired by this work, designing conversion electrodes that can self-form a stable electrochemical system during discharge/charge cycling is a most promising approach to achieve superior lithium-storage properties.

4. Experimental Section

Materials Synthesis: GO was prepared from natural graphite powder via a modified Hummers method.[19,58] The GO product was collected and washed thoroughly using a mixed aqueous solution of 3 wt% H_2SO_4/0.5 wt% H_2O_2, followed by deionized (DI) water until the pH value was 4.[25] An aqueous exfoliated GO suspension (200 mL, approximately 200 mg) was obtained by dispersing the resultant mixture in DI water under ultrasonication for 5 h. A solution of $Mn(CH_3COO)_2{\cdot}4H_2O$ (100 mL 100 mM) was added to the above suspension under stirring, followed by adding 5 mL of hydrazine hydrate (80 wt%). The mixture was further stirred for 24 h to obtain a Mn-precursor/graphene intermediate. Finally, the MnO/graphene nanocomposite was obtained by annealing the Mn-precursor/graphene hybrid at 500S °C (ramp rate: 1 °C min^{-1}) in a 5% H_2/Ar atmosphere for 5 h. For comparison, bare MnO was also prepared under the same conditions.

Materials Characterization: Powder XRD patterns were recorded on a X'Pert PRO (PANalytical B.V., Holland) X-ray diffractometer using Cu K_1 irradiation (λ = 1.5406 Å). XPS measurements were carried out using a VG MultiLab 2000 system with a monochromatic Al Kα X-ray source (ThermoVG Scientific). The morphology and composition of the samples were characterized by FESEM (FEI, Sirion 200) coupled with an EDX (Oxford Instrument) spectrometer. TEM images were taken with

a JEOL 2100F microscope. Thermogravimetric and differential thermal analyses (TG/DTA) were performed with a PerkinElmer Diamond TG/DTA apparatus at a heating rate of 10 °C min^{-1} in flowing air. Raman spectra were measured on a Renishaw Invia spectrometer using an Ar^+ laser of 514.5 nm at room temperature. Nitrogen adsorption–desorption isotherm measurements were conducted at 77 K using a Micrometritics ASAP 2020 analyzer to determine the BET surface area and porosity.

Electrochemical Measurements: The working electrodes were fabricated by coating a slurry containing 80 wt% active material (MnO/graphene hybrid), 10 wt% acetylene black (Super-P), and 10 wt% polyvinylidene fluoride (PVDF) dissolved in *N*-methyl-2-pyrrolidinone onto a copper foil and dried at 80 °C in vacuum for 6 h before pressing. The coated copper foil was cut into disk electrodes (8 mm in diameter) and further dried at 80 °C for 24 h in vacuum. The electrochemical performance of the active material was examined via 2032 type coin cells with a pure lithium foil as the counter electrode, Celgard 2300 as the separator, and 1 M $LiPF_6$ in a mixture of ethylene carbonate (EC) and dimethyl carbonate (DMC) (v/v = 1:1) as the electrolyte. The test cells were assembled in an argon-filled glovebox with concentrations of moisture and oxygen below 1.0 ppm. A PARSTAT 2273 potentiostat was employed for CV measurements at a scanning rate of 0.2 mV s^{-1} and electrochemical impedance spectrometry tests in a frequency range of 100 kHz to 100 mHz at room temperature. The galvanostatic charge–discharge measurements were carried out using a Land Battery Measurement System (Land, China) under various current densities of 200–3000 mA g^{-1} in the fixed voltage range of 3.00–0.01 V vs. Li/Li^+ at room temperature.

Supporting Information

Supporting Information is available from the Wiley Online Library or from the author.

Acknowledgements

This work was supported by the Natural Science Foundation of China (Grant Nos. 51002057, 21271078 and 50825203), the 863 program (Grant No. 2009AA03Z225), the Natural Science Foundation of Hubei Province (Grant No. 2008CDA026), and the PCSIRT (Program for Changjiang Scholars and Innovative Research Team in University). The authors thank the Analytical and Testing Center of HUST for XRD, FESEM, TEM, and TG-DTA measurements.

Received: September 11, 2012
Revised: October 24, 2012
Published online: December 10, 2012

[1] A. Magasinski, P. Dixon, B. Hertzberg, A. Kvit, J. Ayala, G. Yushin, *Nat. Mater.* **2010**, *9*, 353.
[2] L. X. Yuan, Z. H. Wang, W. X. Zhang, X. L. Hu, J. T. Chen, Y. H. Huang, J. B. Goodenough, *Energy Environ. Sci.* **2011**, *4*, 269.
[3] C. K. Chan, H. Peng, G. Liu, K. McIlwrath, X. F. Zhang, R. A. Huggins, Y. Cui, *Nat. Nanotechnol.* **2008**, *3*, 31.
[4] K. Kang, Y. S. Meng, J. Bréger, C. P. Grey, G. Ceder, *Science* **2006**, *311*, 977.
[5] H. Li, Z. X. Wang, L. Q. Chen, X. J. Huang, *Adv. Mater.* **2009**, *21*, 4593.
[6] P. Poizot, S. Laruelle, S. Grugeon, L. Dupont, J. M. Tarascon, *Nature* **2000**, *407*, 496.
[7] F. D. Wu, Y. Wang, *J. Mater. Chem.* **2011**, *21*, 6636.
[8] W. L. Yao, J. Yang, J. L. Wang, Y. N. Nuli, *J. Electrochem. Soc.* **2008**, *155*, A903.
[9] Y. M. Sun, X. L. Hu, W. Luo, Y. H. Huang, *J. Mater. Chem.* **2012**, *22*, 13826.
[10] X. W. Lou, D. Deng, J. Y. Lee, J. Feng, L. A. Archer, *Adv. Mater.* **2008**, *20*, 258.
[11] Y. G. Li, B. Tan, Y. Y. Wu, *Nano Lett.* **2008**, *8*, 265.
[12] X. J. Zhu, Y. W. Zhu, S. Murali, M. D. Stoller, R. S. Ruoff, *ACS Nano* **2011**, *5*, 3333.
[13] Z. Y. Wang, D. Y. Luan, S. Madhavi, Y. Hu, X. W. Lou, *Energy Environ. Sci.* **2012**, *5*, 5252.
[14] B. Wang, J. S. Chen, H. B. Wu, Z. Y. Wang, X. W. Lou, *J. Am. Chem. Soc.* **2011**, *133*, 17146.
[15] P. L. Taberna, S. Mitra, P. Poizot, P. Simon, J. M. Tarascon, *Nat. Mater.* **2006**, *5*, 567.
[16] E. Kang, Y. S. Jung, A. S. Cavanagh, G. H. Kim, S. M. George, A. C. Dillon, J. K. Kim, J. Lee, *Adv. Funct. Mater.* **2011**, *21*, 2430.
[17] G. M. Zhou, D. W. Wang, F. Li, L. L. Zhang, N. Li, Z. S. Wu, L. Wen, G. Q. Lu, H. M. Cheng, *Chem. Mater.* **2010**, *22*, 5306.
[18] X. W. Lou, Y. Wang, C. L. Yuan, J. Y. Lee, L. A. Archer, *Adv. Mater.* **2006**, *18*, 2325.
[19] S. M. Paek, E. Yoo, I. Honma, *Nano Lett.* **2008**, *9*, 72.
[20] H. Liu, G. X. Wang, J. Liu, S. Z. Qiao, H. Ahn, *J. Mater. Chem.* **2011**, *21*, 3046.
[21] X. H. Huang, J. P. Tu, Z. Y. Zeng, J. Y. Xiang, X. B. Zhao, *J. Electrochem. Soc.* **2008**, *155*, A438.
[22] H. L. Wang, L. F. Cui, Y. Yang, H. Sanchez Casalongue, J. T. Robinson, Y. Y. Liang, Y. Cui, H. J. Dai, *J. Am. Chem. Soc.* **2010**, *132*, 13978.
[23] J. Gao, M. A. Lowe, H. D. Abruña, *Chem. Mater.* **2011**, *23*, 3223.
[24] Y. M. Sun, X. L. Hu, J. C. Yu, Q. Li, W. Luo, L. X. Yuan, W. X. Zhang, Y. H. Huang, *Energy Environ. Sci.* **2011**, *4*, 2870.
[25] Y. M. Sun, X. L. Hu, W. Luo, Y. H. Huang, *ACS Nano* **2011**, *5*, 7100.
[26] W. Luo, X. L. Hu, Y. M. Sun, Y. H. Huang, *Phys. Chem. Chem. Phys.* **2011**, *13*, 16735.
[27] Y. M. Sun, X. L. Hu, W. Luo, Y. H. Huang, *J. Mater. Chem.* **2012**, *22*, 425.
[28] K. J. Zhang, P. X. Han, L. Gu, L. X. Zhang, Z. H. Liu, Q. S. Kong, C. J Zhang, S. M. Dong, Z. Y. Zhang, J. H. Yao, H. X. Xu, G. L. Cui, L. Q. Chen, *ACS Appl. Mater. Interfaces* **2012**, *4*, 658.
[29] K. F. Zhong, X. Xia, B. Zhang, H. Li, Z. X. Wang, L. Q. Chen, *J. Power Sources* **2010**, *195*, 3300.
[30] K. F. Zhong, B. Zhang, S. H. Luo, W. Wen, H. Li, X. J. Huang, L. Q. Chen, *J. Power Sources* **2011**, *196*, 6802.
[31] X. P. Fang, X. Lu, X. W. Guo, Y. Mao, Y. S. Hu, J. Z. Wang, Z. X. Wang, F. Wu, H. K. Liu, L. Q. Chen, *Electrochem. Commun.* **2010**, *12*, 1520.
[32] M. S. Wu, P. C. J. Chiang, J. T. Lee, J. C. Lin, *J. Phys. Chem. B* **2005**, *109*, 23279.
[33] Y. M. Liu, X. Y. Zhao, F. Li, D. G. Xia, *Electrochim. Acta* **2011**, *56*, 6448.
[34] C. T. Hsieh, C. Y. Lin, J. Y. Lin, *Electrochim. Acta* **2011**, *56*, 8861.
[35] X. Q. Yu, Y. He, J. P. Sun, K. Tang, H. Li, L. Q. Chen, X. J. Huang, *Electrochem. Commun.* **2009**, *11*, 791.
[36] B. Sun, Z. X. Chen, H. S. Kim, H. Ahn, G. X. Wang, *J. Power Sources* **2011**, *196*, 3346.
[37] J. Liu, Q. M. Pan, *Electrochem. Solid-State Lett.* **2010**, *13*, A139.
[38] Y. L. Ding, C. Y. Wu, H. M. Yu, J. Xie, G. S. Cao, T. J. Zhu, X. B. Zhao, Y. W. Zeng, *Electrochim. Acta* **2011**, *56*, 5844.
[39] S. Y. Liu, J. Xie, Y. X. Zheng, G. S. Cao, T. J. Zhu, X. B. Zhao, *Electrochim. Acta* **2012**, *66*, 271.
[40] Y. J. Mai, D. Zhang, Y. Q. Qiao, C. D. Gu, X. L. Wang, J. P. Tu, *J. Power Sources* **2012**, *216*, 201.
[41] Y. M. Sun, X. L. Hu, W. Luo, Y. H. Huang, *J. Mater. Chem.* **2012**, *22*, 19190.
[42] A. K. Geim, K. S. Novoselov, *Nat. Mater.* **2007**, *6*, 183.
[43] Z. S. Wu, W. C. Ren, L. Wen, L. B. Gao, J. P. Zhao, Z. P. Chen, G. M. Zhou, F. Li, H. M. Cheng, *ACS Nano* **2010**, *4*, 3187.
[44] C. X. Peng, B. D. Chen, Y. Qin, S. H. Yang, C. Z. Li, Y. H. Zuo, S. Y. Liu, J. H. Yang, *ACS Nano* **2012**, *6*, 1074.
[45] Y. M. Sun, X. L. Hu, W. Luo, Y. H. Huang, *J. Mater. Chem.* **2011**, *21*, 17229.

[46] J. F. Moulder, W. F. Stickle, P. E. Sobol, K. D. Bomben, *Handbook of X-ray Photoelectron Spectroscopy*, (Ed: J. Chastain), Perkin-Elmer Corporation, Eden Prairie, MN **1992**.
[47] S. Stankovich, R. D. Piner, X. Q. Chen, N. Q. Wu, S. T. Nguyen, R. S. Ruoff, *J. Mater. Chem.* **2006**, *16*, 155.
[48] H. C. Schniepp, J. L. Li, M. J. McAllister, H. Sai, M. Herrera-Alonso, D. H. Adamson, R. K. Prud'homme, R. Car, D. A. Saville, I. A. Aksay, *J. Phys. Chem. B* **2006**, *110*, 8535.
[49] F. Tuinstra, J. L. Koenig, *J. Chem. Phys.* **1970**, *53*, 1126.
[50] O. Delmer, P. Balaya, L. Kienle, J. Maier, *Adv. Mater.* **2008**, *20*, 501.
[51] J. C. Guo, Q. Liu, C. S. Wang, M. R. Zachariah, *Adv. Funct. Mater.* **2012**, *22*, 803.
[52] H. Xia, M. Lai, L. Lu, *J. Mater. Chem.* **2010**, *20*, 6896.
[53] J. Gao, M. A. Lowe, H. D. Abruña, *Chem. Mater.* **2011**, *23*, 3223.
[54] N. G. Rudawski, B. L. Darby, B. R. Yates, K. S. Jones, R. G. Elliman, A. A. Volinsky, *Appl. Phys. Lett.* **2012**, *100*, 0833111.
[55] P. Balaya, H. Li, L. Kienle, J. Maier, *Adv. Funct. Mater.* **2003**, *13*, 621.
[56] J. Jamnik, J. Maier, *Phys. Chem. Chem. Phys.* **2003**, *5*, 5215.
[57] R. Dedryvère, S. Laruelle, S. Grugeon, P. Poizot, D. Gonbeau, J. M. Tarascon, *Chem. Mater.* **2004**, *16*, 1056.
[58] W. S. Hummers, R. E. Offeman, *J. Am. Chem. Soc.* **1958**, *80*, 1339.